Remote Forcing of Internal Waves in Regional Oceanic Models

M.J. Molemaker[1], P. Damien[1], D. Dollery[1], and J.C. McWilliams[1]

[1]UCLA, Dept. Atmospheric and Oceanic Sciences, Los Angeles, CA

Key Points:

- Remotely forced internal waves are essential to obtain realistic internal wave energies in regional oceanic models.
- Online interpolation of data for nested solutions provide high frequency updates at open boundaries of the regional domain.
- New boundary conditions for open boundaries are introduced that provide the correct level of internal wave energy while avoiding excess energy due to reflections.

Corresponding author: M. Jeroen Molemaker, `nmolem@atmos.ucla.edu`

Abstract

Regional oceanic general circulation models with nested grids are an essential approach to allow the use of higher grid resolutions. High resolution is required for the study of smaller scale processes, such as submesoscale currents and the internal wave field, in particular the baroclinic tide. Limits of available computing power determine the size of the computational grid, setting the maximum size of the modeled domain. A serious problem arises because internal waves can propagate over long distances, providing a remotely forced component for the wave field in any model that doesn't cover a complete oceanic basin. Current approaches in regional oceanic modeling are not adequate. The often used approach of radiative-restoring boundary conditions that work well for flows at sub-inertial time-scales are inadequate to force sufficiently energetic high-frequency internal waves. Prescribed (or "clamped") boundary conditions are susceptible to spurious reflection of energy at the boundaries, leading to an overestimate of internal wave energy inside the regional model domain. We propose a combination of a dynamic tuning between propagating and externally prescribed boundary conditions based on matching the vertically-integrated, high-frequency pressure flux across an open boundary. We show that this approach provides accurate internal wave energy fluxes at the boundaries of the regional domain. This innovation is both necessary and sufficient to investigate the dynamics of the internal wave field continuum and its interactions with submesoscale flows at the high spatial resolutions that regional oceanic models allow.

Plain Language Summary

A new type of open boundary condition is introduced for oceanic models that allows for remote forcing of internal tides and waves while avoiding excessive reflections at the boundaries, in addition to previously developed procedures for allowing outward propagation and incoming large-scale influences.

1 Introduction

Our ability to simulate small-scale oceanic phenomena such as submesoscale currents, internal waves, and turbulent processes leading to dissipation in global oceanic models is limited by finite computing resources. Regional models provide a means to access higher resolutions by reducing the physical area of computation. To force these regional models at their lateral boundaries, open boundary conditions (OBCs) are employed that use information from an oceanic climatology, or a previously computed simulation at larger scales. These boundary conditions serve to make the mathematical problem well posed and to provide information from the outer "parent" solution to the nested inner "child" solution with finer grid resolution. When done successfully, this approach makes it possible to simulate smaller scale currents under the down-scaling hypothesis of emergent phenomena under larger-scale influence. A good starting point for boundary conditions at open boundaries for regional oceanic models is in Marchesiello et al. (2001).[1]

At a fundamental level, the ocean is a continuous fluid between a solid boundary and a free surface, hence an open boundary in its interior is artificial. Therefore, OBCs are also artificial, and their utility is to be judged by the properties of the fluid solutions that result.[2] Many studies have made use of OBCs with one-way nesting. These include forcing by external values at the boundary and radiating wave energy out of the domain by specifying the wave speed there. This has been applied to surface gravity waves (Chapman,

---

[1] Coupled, evolving, parent-child grids (a.k.a. two-way nesting) are also possible (Debreu & Blayo, 2008), but this approach is less widely practiced and, in many situations, it has an uncertain added value over the simpler one-way nesting.

[2] "All models are wrong but some are useful." (George Box)

1985), atmospheric gravity waves (Klemp & Durran, 1983), and hydrostatic oceanic internal currents and waves (Carter & Merrifield, 2007; Marsaleix et al., 2006; Mason et al., 2010; Suanda et al., 2018). The limitation of these approaches is that the approximation of wave speeds and vertical and horizontal wavenumbers inevitably leads to errors in the radiative boundary conditions, which lead to spurious waves reflecting into the domain. It can also be computationally expensive to solve for spectral wave number properties (frequency, wavenumber, amplitude) and estimate the propagation speed. A variant of this approach uses an adaptive algorithm in which inward and outward information are treated separately (Marchesiello et al., 2001); this approach is called *advaptive-Orlanski OBCs* as an extension of the radiation OBCs by Orlanski (1976), and it has proved to successfully deal with, *e.g.,* , mesoscale eddies passing through the open boundary (Penven et al., 2006).

In Rogers et al. (2019), an improvement in the OBCs is proposed: to mitigate spurious reflection of internal wave energy at the boundary, an adaptive sponge layer (*i.e.,* damping and smoothing) near the open boundary is applied that depends on the sign of the total baroclinic energy flux of high-frequency energy across the boundary. When the flux is out of the domain, the sponge layer is active to reduce reflections, whereas for a boundary energy flux into the domain, the sponge layer is locally turned off to allow the nested domain to be fully forced by the incoming internal wave spectrum. A variant of this sponge-layer approach is used to manage the incoming wave energy and spurious reflections of the outgoing wave energy at the boundaries (Siyanbola et al., 2023), using a frequency-wavenumber analysis to partition the energy fluxes near the boundary. Beyond quantifying the substantial amount of reflected wave energy, the results are used to optimize the diffusion and viscosity parameters as a compromise between weak damping of incoming waves and large reduction of wave reflections. The approach of Rogers et al. (2019) suffers from the inability to separate the net energy flux into incoming and outgoing partitions, which can lead to an incorrect assessment of the direction of the physical flux due to the existence of spurious reflections in the first place. The approach of Siyanbola et al. (2023), is limited by the fact that a choosing a single value for the damping parameter for the whole domain does not allow the distinction of different areas along the boundaries with different internal wave characteristics. In this paper we propose a novel approach that is intended to alleviate the limitations above and allow for an accurate matching of the high frequency energy fluxes at the boundaries of a nested domain with those of the parent solution; we call this new approach *dynamic-Orlanski OBCs.*

Open boundary conditions for the continuous hydrostatic Boussinesq equations are known to be ill posed (Oliger & Sundström, 1978; Bennett, 1992). Notwithstanding this, the discrete approximation can be stable in situations where information is transported in and out of the domain. As a result, the precise specification of OBCs is often not rigorously founded in theory but results from an engineering approach where the results justify the formulation. Small changes have arisen in the ROMS OBCs while making many nested simulations in the last two decades and are. These changes have not recently been documented, and therefore we show here the formulation of the OBCs as now in the UCLA version of the Regional Oceanic Modeling System (ROMS; Sec. 2. This is the code version that has been used in recent studies such as Kessouri et al. (2021); van der Boog et al. (n.d.); McWilliams et al. (2024) and many others that made use of UCLA-ROMS. The particular advance reported here is the treatment of high-frequency boundary conditions (*e.g.,* tides).

2 Simulation Model

2.1 UCLA ROMS

The UCLA version of ROMS is a hydrostatic, free-surface, terrain-following oceanic model with a split-explicit (*i.e.,* separating barotropic and baroclinic components), predictor-corrector time-stepping scheme and an equation of state for seawater (A. F. Shchepetkin & McWilliams, 2005; A. Shchepetkin & McWilliams, 2009; A. F. Shchepetkin & McWilliams, 2009; A. Shchepetkin & McWilliams, 2011). It uses 3^{rd}-order upwind algorithms for the horizontal advection of tracers and momenta; these schemes have a dissipative discretization error that is hyper-diffusive or viscous in nature and automatically scales with grid resolution, negating the need for an explicitly described horizontal damping term. Vertical advection is computed with a 4^{th}-order spline-based scheme. Unresolved mixing processes are parameterized with the K-profile Parameterization for the surface and bottom boundary layers, combined with a Richardson-number-based parameterization in the interior (Large et al., 1994). The model also has a non-hydrostatic kernel that is based on a multi-grid Poisson solver (Guillaume et al., 2017) and allows for the simulation of smaller-scale physics beyond the hydrostatic approximation (Ho et al., 2021; Hypolite et al., 2023).

2.2 Pacific Basin solution

The basis for the numerical solutions in this paper is a simulation of the entire Pacific Ocean basin with a hyper-mesoscale horizontal grid resolution of $dx = 6$ km. It is a high-resolution descendant of the well-validated simulation in (Lemarié et al., 2012) with high-frequency atmospheric forcing, as well as with additional tidal forcing. Strictly speaking, this is still a regional simulation that needs to be forced at its lateral boundaries, which are most extensive in the south. To generate information for these open boundaries, we use the GLORYS reanalysis data set (Verezemskaya et al., 2021) that provides data at a resolution of 0.083 degree and a time interval of 1 day. The GLORYS data are pre-processed to be interpolated in space to the computational grid of the model. Interpolation in time, from the discrete 1 day interval to the model time at each time-step, is done while the model is running. For later reference, we refer to the latter type of data processing computations as 'online', in contracts with 'offline' computations, which refer to pre- and post-processing of data before or after the model run.

The GLORYS data do not contain tidal information, and the basin-scale simulations are tidally forced at the open boundaries with sea-surface elevations and barotropic tidal currents from the 10 most energetic tidal frequencies from the TPXO9 analysis (Egbert & Erofeeva, 2002). In addition to this tidal forcing at the lateral boundaries, the model is forced by a surface geopotential forcing. The surface geopotential is a combination of the astronomical tide and the self-attraction and loading correction. self-attraction and loading corrections are the result of geopotential anomalies that arise from the evolving elevation of the sea surface itself, as well as the deformation of the Earth's crust under the influence of tidal motions (Arbic, 2022).

Atmospheric forcing is obtained from the ERA5 global reanalysis (Hersbach et al., 2020). This dataset is available at a nominal 0.25 degree spatial resolution and hourly intervals. The COARE formulation (Fairall et al., 1996) is used to compute momentum and tracer fluxes from atmospheric variables at the surface of the ocean using a bulk approach. The use of sufficiently high-frequency atmospheric forcing allows realistic levels of near-inertial and tidal internal waves below the mixed layer, which are essential to a correct representation of the kinetic energy budget in the ocean (Shcherbina et al., 2013; Barkan et al., 2024). Results that assess the high-frequency OBCs in the Pacific are in section 4. More complete descriptions of the tidal behavior in this simulation are in McWilliams et al. (2024); Damien et al. (2025); Molemaker et al. (2026).

2.3 Sequentially nested subdomains

To achieve the high grid resolutions that are needed to better resolve the submesoscale, internal wave, and turbulent mixing processes, a series of nested numerical subdomains is used. At each stage of nesting, data for the governing variables at the boundaries of the nested grid are interpolated online during the computation of the parent grid and output at 30 minute intervals. The high temporal resolution of the boundary date makes it possible to directly force internal waves and tides in the nested domain without undue loss of variance. Using identical model formulations for both the parent and child grids provides maximal dynamical consistency between the two solutions, which in turn minimizes numerical artifacts near the open boundaries of the child domain. The only changes in dynamics are the result of changes in spatial resolution between the solutions of the two nested domains. Higher resolution means that horizontal dissipation occurs on smaller scales, allowing additional phenomena to be resolved. Since the changes in dynamical regime are a function of the ratio between the grid spacing of the nested grids, it is advisable to keep this relatively small. Although there is obviously no hard and fast rule, we have adopted a nesting resolution ratio of $3:1$. Based on many previous nesting solutions, this has proven to avoid most numerical artifacts at the open boundaries. In addition, we keep to the practices described in Mason et al. (2010), matching the topographies and land masks of the nested domains at the boundaries of the nested subdomain.

In this paper, we present results from two subdomains, in the Northwest and Northeast sectors of the Pacific, each with a horizontal grid resolution of $dx = 2$ km (Sec. 4).

3 Open boundary conditions

For a fluid-dynamical Partial Differential Equation system with open horizontal boundaries, many different choices of the OBCs can be used. For idealized problems intended as process studies, some plausible choices might be Neumann, Dirichlet, or periodic OBCs for the dependent variables. However, for more realistic simulations, our focus in this paper, these OBCs do not adequately represent the essential phenomena of allowing internally-generated outgoing signals to leave the domain and externally-specified incoming signals to provide the larger-scale environmental context, usually through grid nesting (section 2.3). The latter type of OBCs are the subject of this section.

ROMS has curvilinear spatial coordinates (ξ, η, s), where s is the terrain-following vertical (gravity-aligned) coordinate. Discretely, these coordinates have grid indices (i, j, k). For the horizontal OBCs, s and k are implicit and need not be considered further. For simplicity, we express the horizontal coordinates as Cartesian (x, y) with indices (i, j), grid spacings (dx, dy), and velocities (u, v). For brevity, we write the OBC formulas only for the left boundary at $x = 0$, with analogous conditions for the other three boundaries. The complete documentation is in the code itself (see the Open Research Section).

ROMS uses a C-grid, where horizontal momenta are located at cell faces, and the first u-point is located on the boundary at $i = 0$ (Fig. 1). At this boundary, the tangential velocity v, and the tracers T are defined starting at $i = -1/2$ in a virtual buffer to facilitate the specification of boundary conditions at $x = 0$. Throughout the domain, u velocity values are located at $i \in [0..N_x]$ and v, and T values are located at $i - 1/2 | i \in [0..N_x + 1]$. The prognostic u, v and T variables are 3-dimensional and therefore also a function of the vertical k index. When needed, simple averaging of variables to the specified i, j locations is assumed. Finally, the time level of variables is indicated with a superscript n. The interior variables are advanced to the new time level $n + 1$, and the boundary conditions are applied afterward to advance the values on the boundary and in the virtual buffer to the new time level.

In this section, the OBC design principles are expressed in continuous and semi-discrete forms while eliding details of the split-explicit, predictor-corrector time-stepping scheme; the full discretization formulas in (i, j, n) are in Appendix A.

Unlike the fluid-dynamical equations, the OBCs should be viewed as a necessary but somewhat arbitrary model parameterization, analogous to the interior subgrid-scale

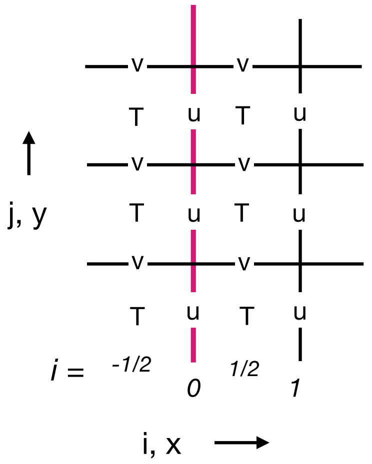

Figure 1. Location of prognostic variables near the left boundary on a C-grid. The boundary of the computational domain is indicated with a solid red line at index $i = 0$. i and j are horizontal indices increasing to the right and upward, u is the normal velocity, v is the tangential velocity, and T is temperature, salinity, or any other material concentration. Each variable has its associated j value.

transport representation. The OBC design principles reflect their desired effects: outgoing transport (a.k.a radiation) across the boundary, incorporation of external environmental influences (a.k.a restoring or nudging), and smoothing and damping of false reflections (a.k.a. sponging).

The **transport equation** at the boundary in continuous form is

$$\partial_t \phi + c_x \partial_x \phi + c_y \partial_y \phi = 0 \,, \tag{1}$$

where ϕ is a prognostic variable and c_x and c_y are projections of the oblique transport velocity, *e.g.,* either through wave propagation or advection. A formal solution of this equation (Raymond & Kuo, 1984) is

$$c_x \to r_x = -\frac{\partial_t \phi \, \partial_x \phi}{(\partial_x \phi)^2 + (\partial_y \phi)^2} \,, \qquad c_x \to r_y = -\frac{\partial_t \phi \, \partial_y \phi}{(\partial_x \phi)^2 + (\partial_y \phi)^2} \,, \tag{2}$$

and this is a useful guide for the OBC discretization.

The **nudging equation** at the boundary in continuous form is

$$\partial_t \phi = -\frac{1}{\tau} \left(\phi - \phi^{ext} \right) \,, \tag{3}$$

where ϕ^{ext} represents external data and τ is a relaxation time.

The **sponging equation** in the neighborhood of the boundary in continuous form is

$$\partial_t \phi = K \nabla^2 \phi \,, \tag{4}$$

where $K(x, y)$ is a smoothing coefficient and ∇ is the horizontal Laplacian operator.

In their discrete forms these three principles are combined as described in the rest of this section. They are treated separately for the 2D barotopic mode and the 3D baroclinic mode and differently each of the prognostic variables. These OBCs are the same in the hydrostatic and nonhydrostatic ROMS codes, with the addition for the latter of w as another prognostic variable (located horizontally at the same (i, j) as T) and of Neumann boundary conditions in the 3D pressure solver.

3.1 Barotropic OBCs

The OBCs used for the barotropic mode derive from Flather (1976) and are adapted in UCLA ROMS in Marchesiello et al. (2001) and Mason et al. (2010) (section 2.1.2). A primary purpose is the representation of barotropic gravity waves, especially the remotely generated external tide. Because it has previously been well described, its implementation details are not presented here. Sec. 4 demonstrates that it continues to perform well in the present Pacific simulation and nested subdomains. The use of a split-explicit time-stepping scheme allows for a small dt value for the barotropic mode, and no doubt this helps with its performance for this phenomenon.

3.2 Baroclinic OBCs

Another literature branch for transport-nudging OBCs derives from Orlanski (1976) . The existing implementation of the 3D adaptive-Orlanski OBCs in UCLA ROMS is similar in spirit to the description in Marchesiello et al. (2001), where a thorough discussion is presented of their history and motivation. Some details of the discrete implementation have since been changed; these are presented here in advance of the high-frequency generalization in section 3.2.3.

3.2.1 Normal velocity

The normal velocity u has a grid node on the left boundary, $x = 0$ and $i = 0$ (Fig. 1). A schematic discrete implementation is presented here with the full (i, j, n) details in Appendix A. After all the other u values have been fully updated at a previous time and at all interior grid points at the new time $n+1$, the new boundary value $u^{n+1}_{0,j}$ is determined from a combined transport-nudging form of (1)-(3):

$$\Delta_t u \;=\; -\left(1 - \mathcal{C}^{ext}_u\right) \cdot \left(R_x \Delta_x u + R_y \Delta_y u \right) \;+\; \mathcal{C}^{ext}_u \cdot u^{ext} \,. \tag{5}$$

The non-dimensional R coefficients are defined as

$$R_x \;=\; -\,\frac{\Delta_t u\, \Delta_x u}{(\Delta_x u)^2 + (\Delta_y u)^2}\,\frac{dt}{dx}\,, \qquad R_y \;=\; -\,\frac{\Delta_t u\, \Delta_y u}{(\Delta_x u)^2 + (\Delta_y u)^2}\,\frac{dt}{dy}\,, \tag{6}$$

The $\Delta_t u$ are forward differences in t, the $\Delta_x u$ are outward differences in x, and the $\Delta_y u$ are forward differences in y. The non-dimensional weighting coefficient between transport and nudging terms in (5) has the form of a Courant number defined by

$$\mathcal{C}^{ext}_u \;=\; \begin{cases} 0 & \text{if } R_x \geq 0 \\ U_b\,\frac{dt}{dx} & \text{if } R_x < 0 \end{cases} \tag{7}$$

for a U_b an incoming normal velocity at the boundary (see Appendix A). Courant numbers are non-negative by definition, and they need to be bounded by approximately 1 for time-stepping stability. With the outgoing x-differencing, $R_x > 0$ implies outgoing transport. The values of $\mathcal{C}^{ext}_u$ can be seen as a weighting coefficient that are restricted to between 0 and 1, with ranging from pure transport when $\mathcal{C}^{ext}_u = 0$ to full nudging to the exterior velocity u^{ext} when $\mathcal{C}^{ext}_u = 1$. (see eq. 5) which therefore is imposed as a strict upper bound in (5). $\mathcal{C}^{ext}_u$ is related to τ in eq. 3 with values close to 1 representing strong nudging or $\sim dt/\tau >> 1$ and $\mathcal{C}^{ext}_u << 1$ is equivalent to weak nudging ($\sim dt/\tau << 1$).

3.2.2 Tangential velocity and tracers

For ϕ equal to either the tangential velocity v or tracers T, the combined transport and nudging OBCs are applied to obtain $\phi^{n+1}_{-1/2,j}$ after previous time and interior grid point values are determined. In contrast to the normal velocity condition (5) with its R coefficients, the transport velocity coefficients C are purely advective:[3]

$$\begin{aligned}\Delta_t\phi &= -\,C_x\Delta_x\phi \,-\, C_y\Delta_y\phi\,, \\ &\qquad\qquad\qquad \text{if } C_x \geq 0 \;\Rightarrow\; C^{ext}_{\phi} \,=\, 0 \\ &= (1\,-\,\mathcal{C}^{ext}_{\phi})\,C_y\Delta_y\phi \,-\, \mathcal{C}^{ext}_{\phi}(\phi_b\,-\,\phi^{ext}),\,, \\ &\qquad\qquad\qquad \text{if } C_x < 0 \;\&\; C^{ext}_{\phi} \,=\, -\,C_x\,,\end{aligned} \tag{8}$$

where

$$C_x \,=\, u_b\frac{dt}{dx}\,, \qquad C_y \,=\, v_b\frac{dt}{dy}\,. \tag{9}$$

The subscript b denotes boundary or near-boundary grid points. Again, $\mathcal{C}^{ext}_{\phi}$ is a weighting factor between transport and nudging contributions with a value between 0 and 1. $\Delta_t\phi$ is a forward difference in t at the virtual buffer grid point (Fig. 1), Δ_x is an outward difference in x, and Δ_y is a forward difference in y.

3.2.3 Dynamic-Orlanski OBCs

As discussed in Sec. 1, adaptive-Orlanski OBCs do not perform satisfactorily when there is high-frequency, baroclinic energy flux across an open boundary. The novel approach in this paper is to partially correct this failing with an extended dynamic-Orlanski OBC.

To separate the high-frequency internal wave signal from the sub-tidal and sub-inertial (a.k.a. slow) motions, we employ a running filter to separate high frequency from low frequency motions. Following the approach in Rogers et al. (2019),

$$\partial_t\phi_{slow} \,=\, \frac{1}{\tau_f}(\phi - \phi_{slow})\,, \tag{10}$$

where τ_f is now a filter timescale, which will be chosen as $T_f = 1\ day$ for the remainder. While this exponential filter is not very sharp in frequency space and is not symmetric in time, it has the great advantage that it can be run in parallel with the computation. The high-frequency signal is the residual,

$$\phi' \,=\, \phi \,-\, \phi_{slow}\,. \tag{11}$$

The high-frequency, baroclinic, depth-integrated horizontal pressure fluxes at the boundary are then defined by

$$F_x \,=\, \int_{z=-h}^{z=\zeta} u'p'\; dz\,, \qquad F_y \,=\, \int_{z=-h}^{z=\zeta} v'p'\; dz\,. \tag{12}$$

Here, (u', v') are the velocity anomalies in the local (x, y) directions, and p' is the pressure anomaly. The anomalies are with respect to their time-filtered, slow values (10), and the vertical means are removed to retain only the baroclinic components. ζ is the sea surface height and h is the resting depth of the ocean. This is the most important flux component for horizontal exchanges in a depth-integrated kinetic energy balance. F is computed for both the parent and child solutions. Using the parent normal flux as F^{ext},

---

[3] In earlier ROMS versions, Rs as in (6) are also used for v and T OBCs, instead of Cs, but the advective form is now preferred.

whenever the diagnosed child flux is too small, the boundary condition shifts the prognostic fields towards the nudging value, and when it is too large, the shift is toward the adaptive-Orlanski value. This is accomplished by modifying $\mathcal{C}^{ext}$ used in Secs. 3.2.1-3.2.2 as follows. A new weighting factor is determined with a nudging toward the normal-direction energy flux correction by

$$\partial_t \mathcal{C}_{dyn} = \frac{1}{\tau_f} \frac{F^{ext} - F}{F_0} \,. \tag{13}$$

$F_0 = 1$ kW/m is a normalization factor on the order of the fluxes found in the simulated fluxes (Sec. 4, and the nudging time scale $\tau_f = 1$ day is chosen to be the same as the filter scale in (10). These two quantities are both somewhat arbitrary, and they appear as their product in (13); experimentation has shown only a moderate sensitivity to these choices. Note that (13) does not provide a sharp bound on the magnitude or even the sign of C_{dyn}. After determining $\mathcal{C}_{dyn}$, the next step is to define a corrected $\mathcal{C}^{ext}$ value from the relation,

$$\mathcal{C}^{ext}_{\phi} = \min[\,\max[\,\mathcal{C}^{ext}_{\phi}\,,\,\mathcal{C}_{dyn}\,,\,1\,]\,]\,, \tag{14}$$

applied separately for all three $\phi = (u, v, T)$ fields. The condition (14) assures that the output nudging be as strong as indicated by the any of the input $\mathcal{C}$ values while remaining bounded by 1. The condition (13) does not require that $\mathcal{C}_{dyn}$ itself remain within the $[0, 1]$ range, but (14) ensures that $\mathcal{C}^{ext}$ remains with this range, which is a necessary property for a weighting coefficient.

The coefficients $\mathcal{C}$ are a function of the along-boundary coordinate, so the incoming energy flux in the child is tuned to match the fluxes from the parent independently for each location at the boundaries. This makes it possible to deal with varying conditions of incoming, outgoing, and reflecting fluxes at all locations. Notice that for $\mathcal{C}_{dyn} = 0$, we regain the adaptive-Orlanski conditions, whereas for $\mathcal{C}_{dyn} > 1$, the specified external values are used in the OBCs.

3.2.4 Sponge layers

Regardless of which OBC is used, a sponge layer is employed near the open boundaries in the child subdomain to reduce accumulation of energy and to spatially smooth the interior solution to bring it more in line with the coarser resolution fields in the parent solution at the boundaries. It has the additional benefit of mitigating the emergence of an artificial tangential current along the edge of the subdomain (Mason et al. (2010), Sec. 1.2).

The sponge layer is a discretized form of (4) with non-zero K only near the open boundary and with its values reducing to zero linearly with the normal distance from the boundary. In practice, we often use a relatively narrow sponge layer 15 grid points wide. The maximum value of K depends on the grid size. It is chosen such that the diffusive Courant condition,

$$dt < \frac{dx^2}{K} \,, \tag{15}$$

does not impose an additional restriction on the time step size. Because the advective Courant stability limit, $dt < dx/U$,depends linearly on the grid spacing, this implies a further limit on the maximum allowable K; *i.e.,* $K < \alpha\, dx$. In practice, the Courant limit in the interior is often determined by the phase speed of the fastest, mode 1, internal baroclinic modes, which can be as high as 4 m/s. In our usual practice, often the maximum permissible value for K is used. For the 2 nested domains with $\Delta x = 2\ km$ in the Pacific that are discussed here, we use a value of $K = 600\ m^2/s$.

3.2.5 Online extraction of boundary data

In practice, we often find that we are limited more by the amount of data produced by high-resolution models than by the computing power. To downscale high frequency signals into nested computational subdomain, we save information for the subdomain boundaries every 30 minutes (*e.g.,* with good tidal resolution). Traditionally, one might save a 3D output file with the required variables; however, UCLA ROMS is modified to interpolate the necessary external data to the required 2D locations and to save it at the required times, thereby greatly reducing the offline storage. Because F^{ext} is required in (13)-(14), this 2D field is also saved to the subdomain boundary data file.

4 Results

We now analyze the tidal and/or high-frequency (HF) response in the Pacific basin simulation (Sec. 2.2 and assess the capability of the OBCs to downscale these signals into two nested subdomains (Sec. 2.3 in the northeast and northwest Pacific, designated as NEPAC and NWPAC, respectively.

A dominant HF signal is the tide, especially the lunar semi-diurnal (M2) component with its frequency of 2.2×10^{-5} s^{-1}. Figure 2 shows the surface tidal response in the Pacific. Both its amplitude and phase match known tidal solutions (*e.g.,* Egbert and Erofeeva (2002)) quite well with an rms error of only a few centimeters over the whole basin (not shown). The right panel shows the response in the nested NEPAC domain. The barotropic surface response in the nested domain is controlled by the Flather OBCs (Mason et al., 2010). The figure shows that the use of these OBCs, in combination with the high-frequency updates of the boundary information extracted from the parent solution (Sec. 3.2.5), performs well, with only very minor mismatches at the boundaries of the nested domain.

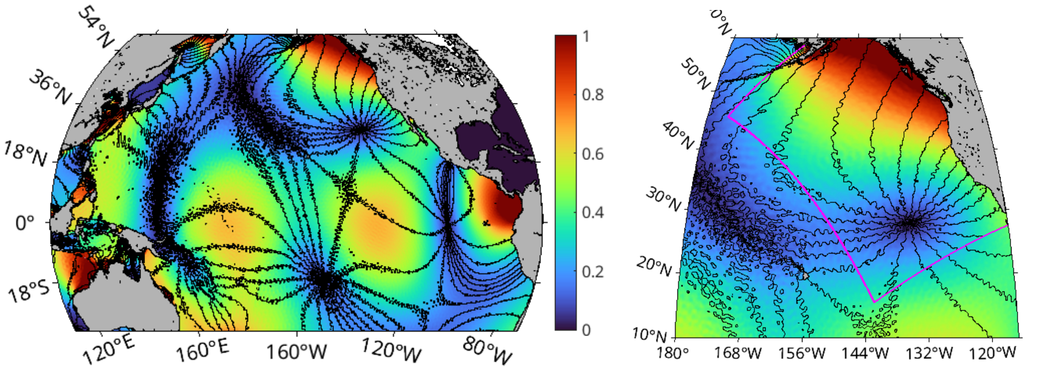

Figure 2. M2 surface tide in the Pacific (left panel). The color scale shows the tidal amplitude [m] and the black lines are iso-phases. The large scale pattern is primarily the barotropic tide. The phase lines are somewhat irregular due to the surface signature of internal tides. The right panel shows a closeup of the northeast Pacific, where the solution from the NEPAC subdomain (indicated by straight maroon lines) is overlaid on the full-basin solution. The downscaling in these fields is almost flawless, with only small mismatches at the open boundaries.

For the remainder of this section, the analysis focuses on the vertically-integrated high-frequency (HF), baroclinic energy fluxes, F in (12). The annually-averaged F fields are in Fig. 3. The zonal fluxes in the left panel reveal that the Pacific basin is dominated by eastward HF fluxes ($F_x > 0$): some well known hot spots of generation are the Hawaiian Islands, Polynesia, and Luzon strait, located in the far Western Pacific around a latitude of $20^o N$. Also indicated in Fig. 3 are the locations of the NEPAC and NWPAC subdomains. In the NWPAC region the internal tide generation is dominated by Luzon Strait. As a result, the F_x are are predominantly outward from that location, both through the western side into the South China sea and out of the eastern side into the broader Pacific. The F_y are mostly to the south in the western Pacific. In contrast, the NEPAC region is dominated by eastward HF energy fluxes into the domain, with remote generation as a significant source of HF energy.

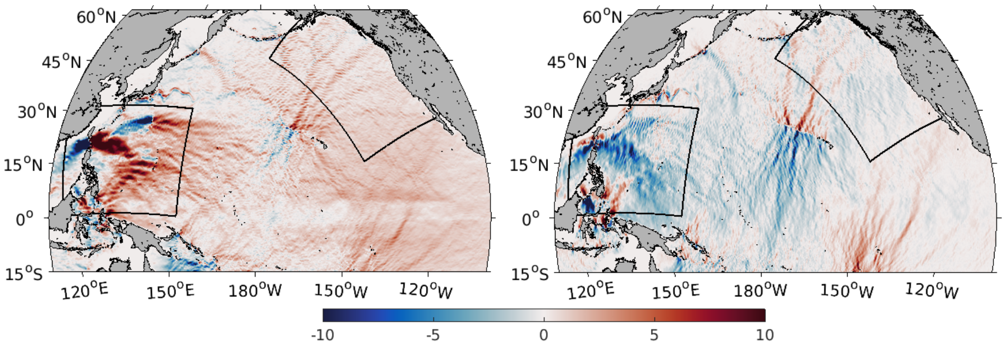

Figure 3. Vertical integral of high-frequency (HF) baroclinic tide and internal wave energy fluxes [kW/m], averaged over a 1 year period (2012) in the Pacific basin (parent) solution: zonal F_x (left panel) and meridional F_y (right panel) energy fluxes. In black are the locations of the two nested subdomains (children), NEPAC and NWPAC, that can be forced with the basin-scale solution at their open boundaries.

The primary topic of this paper is the downscaling the HF baroclinic signal through OBCs. However, it is also important that the OBCs work well for the sub-tidal motions. To illustrate that the new procedures in Sec. 3 do not degrade the low-frequency signals, Fig. 4 shows a snapshot of the temperature and speed at the surface on 1 October, 2017 as a combination of the solutions from the whole Pacific domain and the NWPAC subdomain; the patterns in both of these fields are mostly indicative of the low-frequency components of the simulation. In general these fields show good continuity across the subdomain boundary. There are a few discontinuities visible along the western boundary in the South China Sea. Because of the chaotic evolution of oceanic eddies, the nested solution may evolve into a different turbulent state compared to the parent, leading to small mismatches, predominantly at outflow boundaries. The boundaries of the nested subdomain are free of spurious rim currents, and the Kuroshio Current remains continuous and well behaved as it meanders into and out of the NWPAC domain along the northern boundary.

In the dynamic-Orlanski OBCs (Sec. 3.2.3), $\mathcal{C}_{dyn}$ is important for weighting between transport and nudging influences. Its behavior is examined for the HF fluxes at the boundaries of the NEPAC subdomain in Fig. 5). The range of $\mathcal{C}_{dyn}$ values is limited to $[-12]$, which is larger than its usable range for $\mathcal{C}^{ext}$ in condition (14. Allowing a larger range of values for $\mathcal{C}_{dyn}$ allows it to more adequately match the HF fluxes during periods where the HF flux in the child domain lags behind the changes in the parent HF fluxes. Also shown in Fig. 5 are the HF energy fluxes along the boundaries of the child and parent domains. They track each other well, although there are still some differences at shorter time and length scales mainly along the child boundary. The nudging character of the $\mathcal{C}_{dyn}$ condition (13) is designed to enforce parent-child flux correspondences only on time

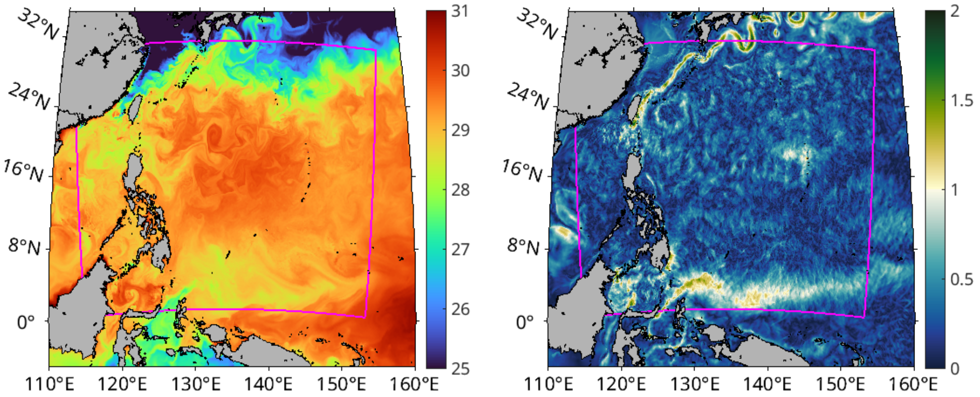

Figure 4. Snapshot of basin-scale and nested solutions at the oceanic surface in the Western Pacific on October 1, 2017. The solid black lines show the boundary of the nested Northwest Pacific subdomain. Outside the subdomain grid, the parent solutions from the full Pacific solution ($\Delta x = 6\ km$) are shown and inside, the nested child solutions ($\Delta x = 2\ km$) are shown. The left panel shows sea surface temperature [^{o}C], and the right panel shows the magnitude of the surface current [m/s].

scales comparable to τ_f of longer. The western boundary shows fluxes that are generally positive into the domain, with the exception of the northern sector which shows fluxes alternating into or out of the domain. Also evident are the amplitude modulations of the largest positive F_x values on the western boundary that result from the spring-neap cycle in the remotely generated tidal beams; these modulations are are tracked well within the child domain. The fluxes along the southern domain boundary are generally out of the domain and are again well tracked by the fluxes in the child domain. The values of $\mathcal{C}_{dyn}$ are generally larger for the western domain boundary, indicative of the fact that there are incoming HF fluxes, which need OBCs that trend more towards prescribed values (*i.e.,* highly nudged). The southern boundary on average has smaller values for $\mathcal{C}_{dyn}$, consistent weaker local generation of the baroclinic tide and outgoing transport, $F_y < 0$. It is clear that the weighting coefficients $\mathcal{C}_{dyn}$ vary significantly both in space and time. This clearly highlights the limitation of using a uniform tuning parameter, such as used in (Siyanbola et al., 2023)

Figure 6 shows time-mean values for the incoming HF energy fluxes into the NEPAC domain, averaged over the last three months of 2017 (the same as the time range in Fig. 5). For both boundaries, and almost all locations, the adaptive-Orlanski OBCs produce the least amount of HF energy into the domain. This is consistent with the known behavior that these OBCs efficiently radiate away wave energy, but are unable to consistently enforce the incoming HF signals. In contrast, the prescribed OBCs (*i.e.,* with$\mathcal{C}^{ext} = 1$) produce the largest amount of incoming fluxes. Again, this is consistent with the fact that these OBCs can enforce incoming signals at all frequencies, but suffer from spurious reflections of outgoing waves. As designed, the new dynamic-Orlanski OBCs generally track the incoming HF fluxes as they were computed in the parent domain very well for a wide range of incoming and outgoing flux values.

In Fig. 7 the energy fluxes F_x (top row) and F_y (bottom row) are shown, again averaged over the last 3 months of 2017 and for the NEPAC area. In this figure, the HF energy fluxes are shown throughout the subdomain, not just at the boundaries. Notice the narrower colorbar scale range in this figure, compared to Fig. 3, which accentuates the patterns. In combination with Fig. 6, this provide additional evidence of the perfor-

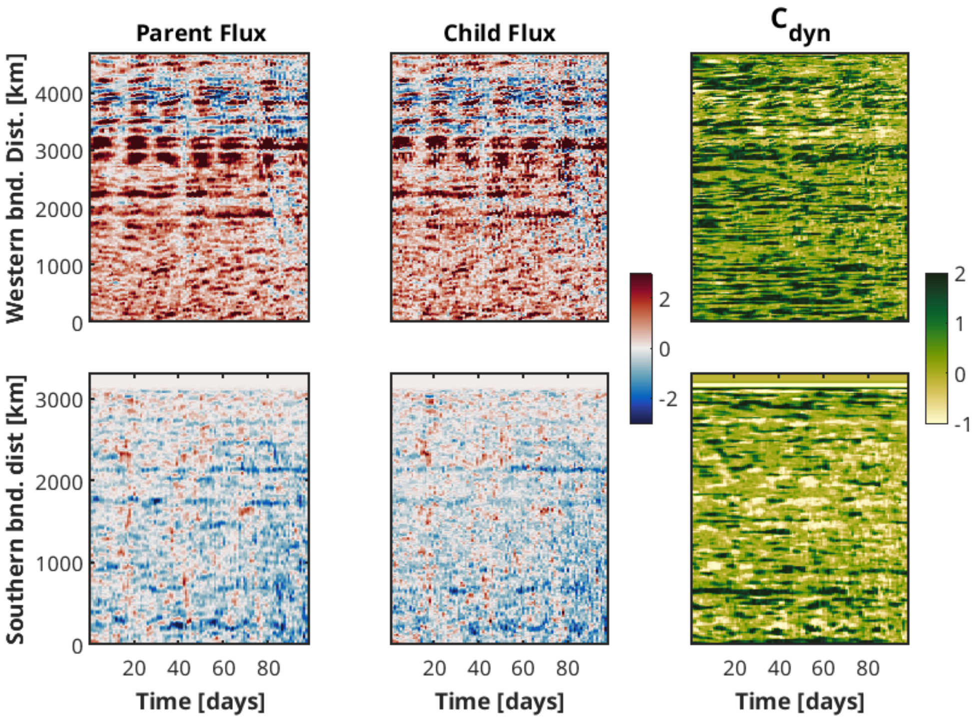

Figure 5. HF energy fluxes F [kW/m] (left two columns, top colorbar) and $\mathcal{C}_{dyn}(t)$ (final column, bottom colorbar) at the boundaries of the NEPAC nested subdomain. The top and bottom rows show the western and southern boundaries, respectively. In the left column, the HF fluxes from the parent grid are shown, and the middle column shows the fluxes from the child grid as a function of time for a period of 70 *days* since September 25, 2017. (horizontal axis). The vertical axis for all the figures shows the location along the boundaries, starting at the South-West corner. The right column shows the coincident variation in space and time of $\mathcal{C}_{dyn}(t)$.

mance of the different OBCs. Clearly, the adaptive-Orlanski OBCs provide too little remotely generated HF energy coming in from the west, so much so that that the sign of F_x is actually reversed. There is barotropic to baroclinic tidal energy conversion at the coastal shelf break and the Mendocino ridge within the NEPAC subdomain, and this locally produced energy leads to outgoing fluxes toward the west. The prescribed OBCs produce an overestimate of incoming fluxes, due to spurious reflections at the western and southern boundaries. The dynamic-Orlanski OBCs yield fluxes much closer to the parent fluxes near the western boundary. Toward the coast on the eastern side of the subdomain, differences are visible with all of the OBC choices; this is due to the increased local production of baroclinic HF energy with the increased grid resolution in the nested subdomain.

As remarked, the northeast Pacific is dominated by remotely forced internal tides such as generated by the topography around the Hawaiian Islands and the Aleutian Islands that form the southern boundary of the Bering sea. This is evident in the larger-area plot of the energy fluxes in Fig. 8. However, like the previous example, this is not uniformly true, because the southern boundary of the domain is characterized by fluxes that are predominantly outwards of the domain.

The internal tides in the North-Western Pacific are dominated by the generation in the Luzon strait between Taiwan and the Philippines, with the highest rate of forcing of internal tidal energy in the world (Pickering et al., 2015). In addition to Luzon

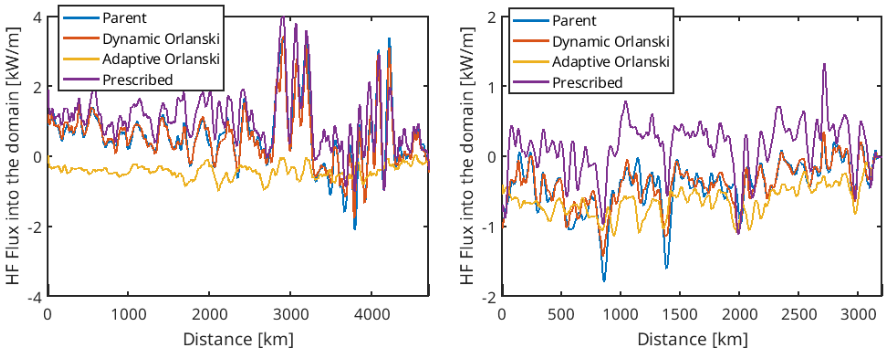

Figure 6. A comparison of the incoming HF energy fluxes [kW/m] into the (left) western edge ($F_x(y)$) and (right) southern edge ($F_y(x)$ the NEPAC subdomain for different OBCs. The fluxes from the parent domain are shown in blue. Using adaptive Orlanski OBCs, the fluxes are typically too negative, reflecting the inability of this OBC to force the nested subdomain with HF data. The prescribed OBCs (*i.e.,* with$\mathcal{C}^{ext} = 1$) lead to too much baroclinic HF energy into the domain: incoming fluxes are transferred well, but outgoing fluxes suffer from reflections at the boundaries. The dynamic Orlanski OBCs track the incoming fluxes very well.

strait, many other island and topographic features in the region are strong generators of internal tides. This is why the the region in figure 9 mostly shows outward HF energy fluxes at the boundaries. However, there are locations along the boundary that show a large amount of baroclinic energy into the nested domain such as the location along the Southern boundary around 130 E (right panel), near the Maluku islands. Our approach not only matching the parent and child domain boundary HF energy fluxes well, it manages to do so without resorting to sponging alone.

5 Summary and limitations

Velocity, tracer, and baroclinic energy flux data are computed on a parent grid and interpolated to A nested subdomain boundary at 30 minute intervals. The cross-boundary baroclinic energy fluxes are filtered in time using a running low-pass filter. A smooth switching function is used to provide a weighted averaging the transport and nudging OBCs and to match the baroclinic energy fluxes between parent and child grids at the boundary of the child domain, followed by moderate smoothing near the boundary using a smoothing operator. Assessments are made of the performance of these dynamic-Orlanski boundary conditions in a Pacific basin simulation with two nested subdomains in the northeast and northwest Pacific. Good continuity is demonstrated across the child boundaries for both low-frequency and high-frequency fields.

Given the general parameterization principles of transport, nudging, flux-matching, and sponging (Sec. 3), the procedure involves several choices for spatial and temporal discreization and for several tuning parameters in the OBCs. These choices are made by trial and error. In these practices, these choices cannot be claimed to be optimal nor even universally applicable to all oceanic regimes; rather, they are sufficiently skillful for the purpose of realistic basin-scale circulations with nested subdomains using the UCLA ROMS code. Most likely, analogous procedures could be made to work well in other circulation models.

A further cautionary remark is the following. Using the dynamic-Orlanski boundary conditions only matches the vertically-integrated baroclinic high-frequency energy

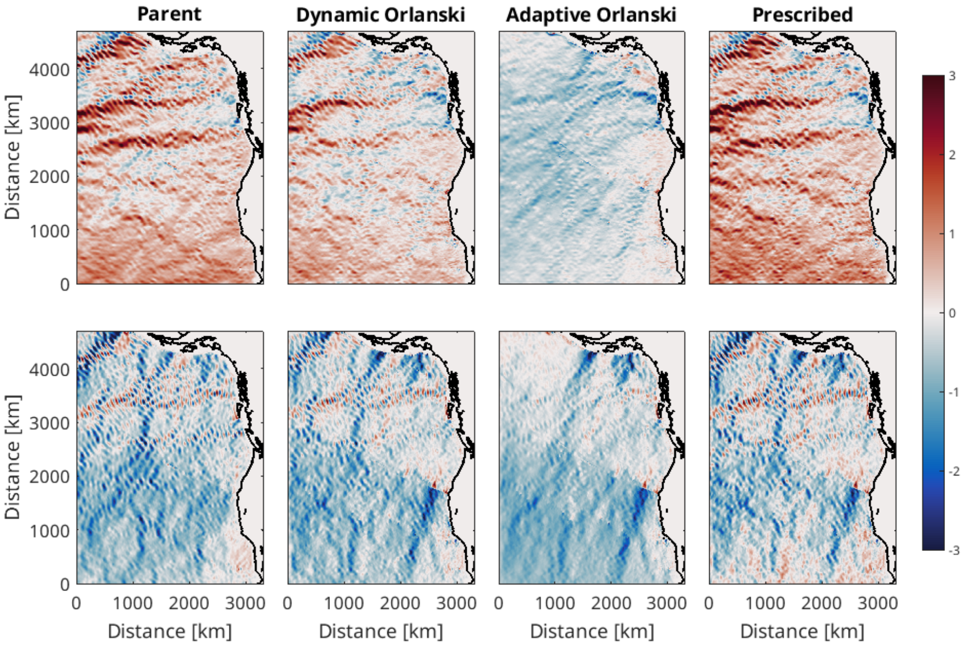

Figure 7. Comparison of the effects of different OBCs on the HF energy fluxes averaged over a three-month period (Oct.-Dec., 2017) for both the parent and child simulations within the area of the NEPAC subdomain. (Top row) F_x [kW/m] and (bottom row) F_y [kW/m]. The nested solution with adaptive-Orlanski OBCs are unable to include the high-frequency forcing of the parent due to remote generation near Hawaii and as a result have a net $F_x < 0$ due to local internal tide generation in the shoaling regions on the western side of the subdomain. The prescribed OBCs overestimate $F_x > 0$ as a result of excessive reflections at the western subdomain boundary. The dynamic-Orlanski OBCs reproduce the F_x fluxes from the parent accurately near the boundary but towards the right, they are reduced as a result of increased generation within the child domain. The F_y differences are less dramatic, but they can be analogously explained.

flux at the boundary in the normal direction. This approach does not explicitly distinguish between outgoing and incoming transport beyond what the original adaptive-Orlanski boundary condition is able to accomplish. If an outgoing wave has a different vertical mode structure compared to an incoming wave, the dynamic-Orlanski approach may not be able to exactly match the partitioning of the wave energy flux into the different modes, but only in the vertical integral. On the other hand, because the OBCs are applied at each vertical level, there will be a nudging toward the vertical structure of the parent solution when the transport is incoming. Attempting to a frequency-wavenumber analysis to decompose the signal into inward- and outward-propagating signals is not only computationally prohibitive, it is also inappropriate for realistically-complex, nonlinearly-interactive currents in nested subdomains with high resolution and small spatial scales. To successfully compute a frequency-wave number analysis, a horizontal scale that is at least equal to the wave length of the first baroclinic mode is needed. For smaller (higher resolution) nested domains, this length scale can approach or exceed the size of the domain, which renders the analysis invalid as a measure of signals 'near' the boundary. For the examples in this paper, this is not a serious limitation because the energy fluxes at larger scales are dominated by the internal waves with a first-baroclinic vertical mode structure (Buijsman et al., 2020), with limited partition into other modes. A possible

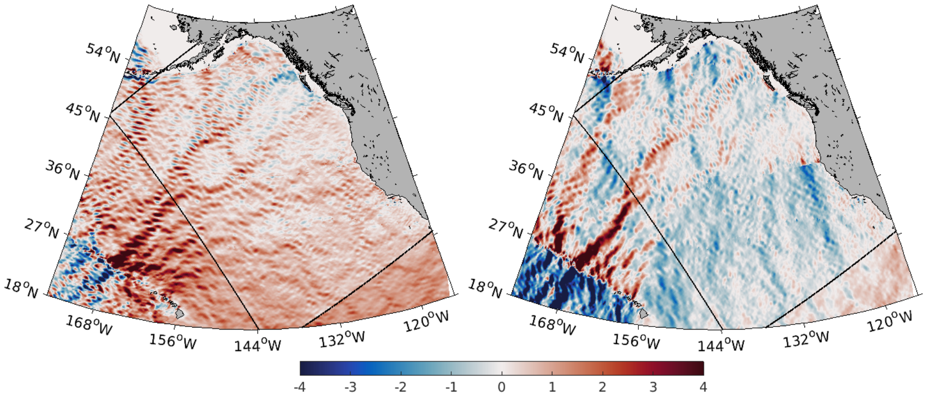

Figure 8. Time-averaged energy fluxes [kW/m] in an eastern Pacific region containing the NEPAC subdomain: (left) zonal F_x and (right) meridional F_y. The black lines indicate the boundaries of the nested subdomain. Outside the confines of the nested sub domain, fluxes from the parent solution are shown, while inside the subdomain, the fluxes computed in the child subdomain are shown. Notice how well the fluxes in the nested domain align with the fluxes from the parent domain at the subdomain boundaries.

extension of the current method would be to decompose the HF fluxes onto baroclinic modes, which would make it possible to match HF energy in different modes independently.

Appendix A Discrete open boundary conditions

Here, we present a more complete description of the discrete implementation of the various open boundary conditions. The open source repository of UCLA ROMS (*https://github.com/CESR-lab/ucla-roms* can also be used as a authoritative reference.

A1 Adaptive Orlanski

The normal velocity at the boundary, following equation 5, can be written as:

$$u^{n+1}_{0,j} = \frac{1-\mathcal{C}_{ext}}{1+r_x}\left[u^n_{0,j} + r_x u^{n+1}_{1,j} - r_y \Delta u_y(0)\right] + \mathcal{C}_{ext} u^{ext}_j \tag{A1}$$

With:

$$r_x = -\frac{\Delta u_t \Delta u_x}{\Delta u_x^2 + \Delta u_y(1)^2}, \tag{A2}$$

$$r_y = -\frac{\Delta u_t \Delta u_y(1)}{\Delta u_x^2 + \Delta u_y(1)^2}, \tag{A3}$$

The value of r_y is limited to the range $[-1, 1]$.

$$\Delta u_t = u^{n+1}_{1,j} - u^n_{1,j}, \tag{A4}$$

$$\Delta u_x = u^{n+1}_{2,j} - u^{n+1}_{1,j}, \tag{A5}$$

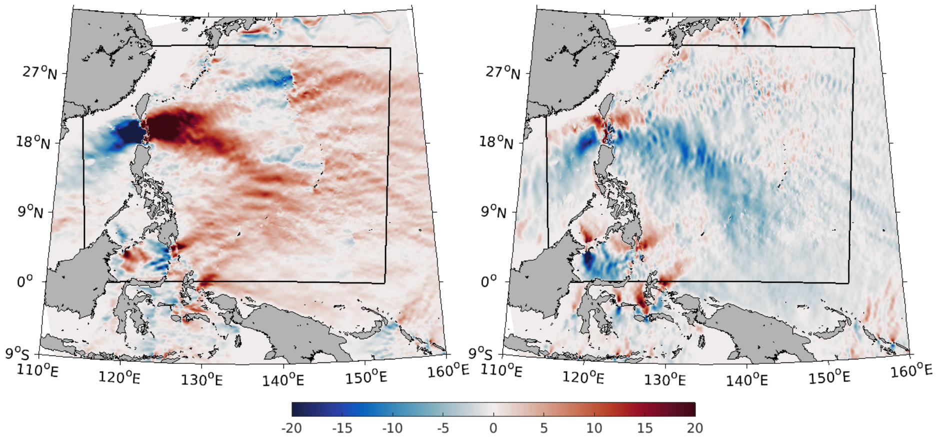

Figure 9. HF baroclinic energy fluxes in the northwestern Pacific, averaged over a 1 month period (December, 2012): (a) zonal F_x [kW/m] and (b) meridional F_y [kW/m]. The black lines indicate the boundaries of the NWPAC subdomain. Outside of the nested subdomain, fluxes from the parent solution are shown, and inside the subdomain the fluxes computed in the child solution are shown. Notice how well the fluxes align with at the boundaries even for this very energetic region of internal tide generation.

$$\Delta u_y(i) = u^n_{i,j+1} - u^n_{i,j,k}, \quad \text{if } \Delta u_t \left(u^n_{i,j+1} - u^n_{i,j-1}\right) > 0, \tag{A6}$$
$$\Delta u_y(i) = u^n_{i,j} - u^n_{i,j-1,k}, \quad \text{if } \Delta u_t \left(u^n_{i,j+1} - u^n_{i,j-1}\right) < 0, \tag{A7}$$

The weights $\mathcal{C}_{ext}$, that determine how strongly the boundary value is nudged towards the externally provided value u^{ext}_j, vary according to:

$$\begin{aligned} \mathcal{C}_{ext} &= 0 && \text{if } r_x > 0, \\ \mathcal{C}_{ext} &= u^{ext}_j \Delta t / \Delta x && \text{if } r_x < 0, u^{ext}_j > 0 \\ \mathcal{C}_{ext} &= u^{bnd} \Delta t / \Delta x && \text{if } r_x < 0, u^{ext}_j < 0 \end{aligned} \tag{A8}$$

Where Δt, and Δx are the time step size and the local grid spacing respectively. u^{bnd} is a parameter to the system and we are using $u^{bnd} = 0.1 m/s$ for all experiments shown. These nudging coefficients are equivalent to using a nudging time scale τ that is based on an advective scaling using $\tau = \Delta x / u$. When the discretely computed phase speed is out of the domain, no nudging towards the external value is applied ($r_x > 0$).

For the normal velocity components at the boundaries, the boundary conditions are formulated as follows. As an example, we show the boundary conditions for the normal velocity u at the left boundary, with similar versions for normal velocities at the other 3 lateral boundaries.

$$u_{bnd} = \frac{1}{1 + r_x} \left[u^n_{1,j,k} + r_x u^{n+1}_{2,j,k} - r_y \Delta u_y(1) \right] \quad \text{if } r_x > 0, \tag{A9}$$

$$u^{n+1}_{1,j,k} = u_{bnd} \quad \text{if } r_x > 0, \tag{A10}$$
$$u^{n+1}_{1,j,k} = (1 - c_{ext}) u_{bnd} + c_{ext} u^{ext} \quad \text{if } r_x < 0. \tag{A11}$$

With:

$$r_x = -\frac{\Delta u_t \Delta u_x}{\Delta u_x^2 + \Delta u_y^2}, \qquad r_y = -\frac{\Delta u_t \Delta u_y(2)}{\Delta u_x^2 + \Delta u_y^2}, \tag{A12}$$

$$\Delta u_t = u_{2,j,k}^{n+1} - u_{2,j,k}^{n}, \qquad \Delta u_x = u_{2,j,k}^{n+1} - u_{3,j,k}^{n+1}, \tag{A13}$$

$$\Delta u_y(i) = u_{i,j+1,k}^{n} - u_{i,j,k}^{n}, \quad \text{if } r_y > 0, \tag{A14}$$
$$\Delta u_y(i) = u_{i,j,k}^{n} - u_{i,j-1,k}^{n}, \quad \text{if } r_y < 0. \tag{A15}$$

The value of r_y is limited to the range $[-1, 1]$.

In the system of equations above, a radiation condition is applied when the discretely computed phase speed is out of the domain (see equation A10). Otherwise, a nudging condition is used on the normal velocity boundary value (eq. A11). The nudging coefficients are:

$$c_{ext} = u^{ext}\Delta t/\Delta x \quad \text{if } u^{ext} > 0, \tag{A16}$$
$$c_{ext} = u^{bind}\Delta t/\Delta x \quad \text{if } u^{ext} < 0. \tag{A17}$$

Where Δt, and Δx are the time step size and the local grid spacing respectively. u^{bind} is a parameter to the system and we are using $u^{bind} = 0.1m/s$ for all experiments shown. These nudging coefficients are equivalent to using a nudging time scale τ that is based on an advective scaling using $\tau = \Delta x/u$.

For tracers and tangential momentum terms, the boundary conditions are as follows. Following the above approach we will show the equations for a variable ϕ at the $i = 0$ boundary. In the definition of the c-grid that is used, the location of the first ϕ value is at $i = -1/2$, in the virtual buffer just outside the domain boundary (see Fig. 1)

$$\phi_{-1/2,j}^{n+1} = (1 - c_x)\left[\phi_{-1/2,j}^{n} - c_y\Delta\phi_y(-1/2)\right] + c_x\left[\phi_{1/2,j}^{n} - c_y\Delta\phi_y(1/2).\right] \quad \text{if } c_x > 0, \tag{A18}$$

$$\phi_{-1/2,j}^{n+1} = (1 - \mathcal{C}_{ext})\left[\phi_{-1/2,j}^{n} - c_y\Delta\phi_y(-1/2)\right] + \mathcal{C}_{ext}\phi^{ext} \quad \text{if } c_x < 0, \tag{A19}$$

Where now $\mathcal{C}_{ext} = -c_x$ and the local Courant numbers c_x, c_y are:

$$c_x = u_{1,j,k}\Delta t/\Delta x, \qquad c_y = 0.5(v_{0,j,k} + v_{0,j+1,k})\Delta t/\Delta y, \tag{A20}$$

And

$$\Delta\phi_y(i) = \phi_{i,j+1,k}^{n} - \phi_{i,j,k}^{n}, \quad \text{if } c_y < 0, \tag{A21}$$
$$\Delta\phi_y(i) = \phi_{i,j,k}^{n} - \phi_{i,j-1,k}^{n}, \quad \text{if } c_y > 0. \tag{A22}$$

A2 Prescribed

The prescribed boundary conditions override values at the boundaries with external data:

$$u_{1,j,k}^{n+1} = u^{ext}, \qquad \phi_{0,j,k}^{n+1} = \phi^{ext} \tag{A23}$$

For velocity components normal to the boundary and tangental components and tracers, respectively. Note that eqs. $(A11, A19)$ revert to prescribed boundary conditions for $c_{ext} = 1$ and $c_x = 1$.

A3 Dynamic Orlanski

The novel approach that is presented in this paper, is a dynamical switching between the two different types of boundary conditions above. Whereas the adaptive Orlanski condition is found to be insufficiently forcing high frequency baroclinic signals, the prescribed boundary condition is found to be too reflective. This realization suggests a hybrid approach between the two types of conditions. Using external data of the incoming high frequency baroclinic energy fluxes, the computed fluxes near the open boundaries are used to match the parent and child high frequency fluxes. Whenever the diagnosed flux into the domain is too small, the model will dynamically switch towards a prescribed boundary condition, whenever the incoming energy flux is too large, it will move more towards adaptive Orlanski as follows:

$$\mathcal{C}_{ext} = max(\mathcal{C}_{ext}, \mathcal{C}_{dyn}) \tag{A24}$$

With:

$$\mathcal{C}^{n+1}_{dyn} = \mathcal{C}^{n}_{dyn} + \frac{1}{\tau}(F_{ext} - F) \tag{A25}$$

In this context, F_{ext} and F are the HF baroclinic energy fluxes as defined in 12, normal to the boundary for the parent and the child domain respectively. It is important to remark that the coefficients $\mathcal{C}_{dyn}$ are a function of the along boundary coordinate, so the incoming flux in the child is tuned to match the fluxes from the parent independently for each location at the boundaries. This makes it possible to deal with varying conditions of incoming, outgoing and reflecting fluxes at all locations. It is easy to see that for $c_{dyn} = 0$, we regain the adaptive Orlanski conditions, whereas for $c_{dyn} = 1$, the prescribed conditions are used.

Open Research Section

The code of UCLA-ROMS is publicly available at *https://github.com/CESR-lab/ucla-roms*.

Acknowledgments

This was research was partially funded by the National Aeronautics and Space Administration grant #80NSSC19K1296-P0000 and the Office of Naval Research grants #N00014-21-1-2693;P00003, #N00014-23-1-2812, #ONR N00014-21-1-2693;P00003, and #N000142412692:P00001

References

Arbic, B. K. (2022). Incorporating tides and internal gravity waves within global ocean general circulation models: A review. *Progress in Oceanography*, *206*, 102824.

Barkan, R., Srinivasan, K., & McWilliams, J. C. (2024). Eddy–internal wave interactions: Stimulated cascades in cross-scale kinetic energy and enstrophy fluxes. *J. Phys. Ocean.*, *54*, 1309 - 1326.

Bennett, A. F. (1992). *Inverse Methods in Physical Oceanography.* Cambridge University Press.

Buijsman, M. C., Stephenson, G. R., Ansong, J. K., Arbic, B. K., Green, J. M., Richman, J. G., … Vic, C. (2020). On the interplay between horizontal resolution and wave drag and their effect on tidal baroclinic mode waves in realistic global ocean simulations. *Ocean Modelling*, *152*, 101656.

Carter, G. S., & Merrifield, M. A. (2007). Open boundary conditions for regional tidal simulations. *Ocean Modelling*, *18*, 194-209.

Chapman, D. C. (1985). Numerical treatment of cross-shelf open boundaries in a barotropic coastal ocean model. *J. Phys. Ocean.*, *15*, 1060 - 1075.

Damien, P., Molemaker, M., McCoy, D., Dollery, D., Guiet, J., Bianchi, D., & McWilliams, J. (2025). Development of a mesoscale- and tide-resolving ocean–biogeochemistry model for the pacific: Tidal enhancement of the biological carbon pump. *JAMES*. (submitted)

Debreu, L., & Blayo, E. (2008). Two-way embedding algorithms: a review. *Ocean Dynamics*, *58*, 415-428.

Egbert, G. D., & Erofeeva, S. Y. (2002). Efficient inverse modeling of barotropic ocean tides. *Journal of Atmospheric and Oceanic Technology*, *19*, 183 - 204.

Fairall, C. W., Bradley, E. F., Rogers, D. P., Edson, J. B., & Young, G. S. (1996). Bulk parameterization of air-sea fluxes for tropical ocean-global atmosphere coupled-ocean atmosphere response experiment. *Journal of Geophysical Research: Oceans*, *101*, 3747-3764.

Flather, R. A. (1976). A tidal model of the north-west European continental shelf. *7th Liege Colloquium on Ocean Hydrodynamics Location, M/'emoires de la Société Royal des Sciences de Liège [0369-1799]*, *10*, 141-164.

Guillaume, R., Jeroen, M. M., Nicolas, D., & Thomas, D. (2017). Compact symmetric poisson equation discretization for non-hydrostatic sigma coordinates ocean model. *Ocean Modelling*, *118*, 107-117.

Hersbach, H., Bell, B., Berrisford, P., Hirahara, S., Horányi, A., Muñoz-Sabater, J., . . . Thépaut, J.-N. (2020). The era5 global reanalysis. *Quarterly Journal of the Royal Meteorological Society*, *146*, 1999-2049.

Ho, M., Molemaker, M. J., Kessouri, F., McWilliams, J. C., & Gallien, T. (2021). Wastewater effluent plume validation using high-resolution nonhydrostatic modeling. *J. Hydraul. Eng.*, *147*, 04021028.

Hypolite, D., Romero, L., McWilliams, J., & Dauhajre, D. (2023). Langmuir circulations transfer kinetic energy from submesoscales to dissipative scales. *J. Phys. Ocean.*, *53*, 253-268.

Kessouri, F., McLaughlin, K., Sutula, M., Bianchi, D., Ho, M., McWilliams, J. C., . . . Leinweber, A. (2021). Configuration and validation of an oceanic physical and biogeochemical model to investigate coastal eutrophication in the Southern California Bight. *Journal of Advances in Modeling Earth Systems*, *13*, e2020MS002296.

Klemp, J. B., & Durran, D. R. (1983). An upper boundary condition permitting internal gravity wave radiation in numerical mesoscale models. *Monthly Weather Review*, *111*, 430 - 444.

Large, W. G., McWilliams, J. C., & Doney, S. C. (1994). Oceanic vertical mixing: A review and a model with a nonlocal boundary layer parameterization. *Reviews of Geophysics*, *32*, 363-403.

Lemarié, F., Kurian, J., Shchepetkin, A. F., Jeroen Molemaker, M., Colas, F., & McWilliams, J. C. (2012). Are there inescapable issues prohibiting the use of terrain-following coordinates in climate models? *Ocean Modelling*, *42*, 57-79.

Marchesiello, P., McWilliams, J. C., & Shchepetkin, A. (2001). Open boundary conditions for long-term integration of regional oceanic models. *Ocean Modelling*, *3*, 1-20.

Marsaleix, P., Auclair, F., & Estournel, C. (2006). Considerations on open boundary conditions for regional and coastal ocean models. *Journal of Atmospheric and Oceanic Technology*, *23*, 1604 - 1613. doi: 10.1175/JTECH1930.1

Mason, E., Molemaker, J., Shchepetkin, A. F., Colas, F., McWilliams, J. C., & Sangrà, P. (2010). Procedures for offline grid nesting in regional ocean models. *Ocean Modelling*, *35*, 1-15.

McWilliams, J. C., Molemaker, M. J., & Damien, P. (2024). Baroclinic sea level. *Journal of Advances in Modeling Earth Systems*, *16*, e2023MS003977.

Molemaker, M. J., Damien, P., McWilliams, J. C., & Dollery, D. (2026). Internal tides in the pacific: A complete energy budget. *J. Phys. Ocean.*.

Oliger, J., & Sundström, A. (1978). Theoretical and practical aspects of some initial boundary value problems in fluid dynamics. *SIAM Journal on Applied Mathematics*, *35*, 419-446.

Orlanski, I. (1976). A simple boundary condition for unbounded hyperbolic flows. *Journal of Computational Physics*, *21*, 251-269.

Penven, P., Debreu, L., Marchesiello, P., & McWilliams, J. (2006). Evaluation and application of the ROMS 1-way embedding procedure to the central California upwelling system. *Ocean Modelling*, *12*, 157-187.

Pickering, A., Alford, M., Nash, J., Rainville, L., Buijsman, M., Ko, D. S., & Lim, B. (2015). Structure and variability of internal tides in luzon strait. *Journal of Phys. Ocean.*, *45*(6), 1574 - 1594.

Raymond, W. H., & Kuo, H. L. (1984). A radiation boundary condition for multi-dimensional flows. *Quarterly Journal of the Royal Meteorological Society*, *110*, 535-551.

Rogers, J. S., Rayson, M. D., Ko, D. S., Winters, K. B., & Fringer, O. B. (2019). A framework for seamless one-way nesting of internal wave-resolving ocean models. *Ocean Modelling*, *143*, 101462.

Shchepetkin, A., & McWilliams, J. (2009). Computational kernel algorithms for fine-scale, multi-process, long-term oceanic simulations. In R. Temam & J. Tribia (Eds.), *Handbook of Numerical Analysis: Computational Methods for the Ocean and the Atmosphere* (Vol. 14, p. 121-183). Elsevier.

Shchepetkin, A., & McWilliams, J. (2011). Accurate Boussinesq oceanic modeling with a practical, “stiffened” equation of state. *Ocean Modelling*, *38*, 41-70.

Shchepetkin, A. F., & McWilliams, J. C. (2005). The regional oceanic modeling system (roms): a split-explicit, free-surface, topography-following-coordinate oceanic model. *Ocean Modelling*, *9*, 347-404.

Shchepetkin, A. F., & McWilliams, J. C. (2009). Correction and commentary for “ocean forecasting in terrain-following coordinates: Formulation and skill assessment of the regional ocean modeling system” by haidvogel et al., j. comp. phys. 227, pp. 3595–3624. *Journal of Computational Physics*, *228*, 8985-9000.

Shcherbina, A. Y., D’Asaro, E. A., Lee, C. M., Klymak, J. M., Molemaker, M. J., & McWilliams, J. C. (2013). Statistics of vertical vorticity, divergence, and strain in a developed submesoscale turbulence field. *Geophysical Research Letters*, *40*, 4706-4711.

Siyanbola, O. Q., Buijsman, M. C., Delpech, A., Renault, L., Barkan, R., Shriver, J. F., … McWilliams, J. C. (2023). Remote internal wave forcing of regional ocean simulations near the u.s. west coast. *Ocean Modelling*, *181*, 102154.

Suanda, S. H., Feddersen, F., Spydell, M. S., & Kumar, N. (2018). The effect of barotropic and baroclinic tides on three-dimensional coastal dispersion. *Geophysical Research Letters*, *45*, 11,235-11,246.

van der Boog, C. G., Molemaker, M. J., Dijkstra, H. A., Pietrzak, J. D., & Katsman, C. A. (n.d.). Generation of vorticity near topography: Anticyclones in the Caribbean sea. *Journal of Geophysical Research: Oceans*, *127*, e2021JC017987.

Verezemskaya, P., Barnier, B., Gulev, S. K., Gladyshev, S., Molines, J.-M., Gladyshev, V., … Gavrikov, A. (2021). Assessing eddying (1/12°) ocean reanalysis GLORYS12 using the 14-yr instrumental record from 59.5°n section in the Atlantic. *J. Geophys. Res. Oceans*, *126*, e2020JC016317.